# Pairing correlations in nuclei on the neutron-drip line

K. Hagino[1] and H. Sagawa[2]
[1]*Department of Physics, Tohoku University, Sendai, 980-8578, Japan*
[2]*Center for Mathematical Sciences, University of Aizu, Aizu-Wakamatsu, Fukushima 965-8560, Japan*
(Received 29 August 2005; published 31 October 2005)

Paring correlations in weakly bound nuclei on the edge of the neutron-drip line is studied by use of a three-body model. A density-dependent contact interaction is employed to calculate the ground state of halo nuclei $^6$He and $^{11}$Li, as well as a skin nucleus $^{24}$O. Dipole excitations in these nuclei are also studied within the same model. We point out that the dineutron-type correlation plays a dominant role in the halo nuclei $^6$He and $^{11}$Li, having the coupled spin of the two neutrons $S = 0$, whereas the correlation similar to the BCS type is important in $^{24}$O. Contributions of the spin $S = 1$ and $S = 0$ configurations are separately discussed in the low-energy dipole excitations.

DOI: 10.1103/PhysRevC.72.044321 PACS number(s): 21.30.Fe, 21.45.+v, 21.60.Gx, 25.60.Gc

## I. INTRODUCTION

It is now feasible to study the structure of nuclei on the edge of neutron-drip line. Such nuclei are expected to have unique properties influenced by the large spatial distribution of weakly bound valence neutrons, for examples, halo, skin, new magic numbers, and strong soft dipole excitations.

Two-neutron halo nuclei (sometimes referred to as Borromean nuclei when there is no bound state between a valence neutron and a core nucleus) like $^6$He and $^{11}$Li have been often described as three-body systems consisting of two valence neutrons interacting with each other and with the core [1–7]. The three-body Hamiltonian with realistic two-body interactions has been solved by the Faddeev method [6,7]. On the other hand, Bertsch and Esbensen have developed a three-body model with a density-dependent $\delta$ interaction among the valence neutrons [1]. They have subsequently extended their model by taking into account the effect of the recoil of the core nucleus [3]. They showed that the density-dependent contact force well reproduces the results of Faddeev calculations even though the radial dependence of the adopted interactions are quite different [3]. To date, the most sophisticated many-body calculations of light nuclei include also three-body forces that play an important role in obtaining the correct binding energies of light nuclei [8]. To a large extent, such three-body forces can also be simulated effectively by a density-dependent force.

Recently, a Hartree-Fock-Bogoliubov (HFB) model has been applied to study a dineutron structure of the drip line nuclei. The dipole response has also been studied with the quasiparticle random-phase approximation (QRPA), taking into account the continuum effect [9]. Cluster models have also been often used to study the Borromean nuclei including the dipole excitations [10,11].

In this paper, we undertake a detailed discussion of the ground state as well as the dipole response of neutron-rich nuclei by using a three-body model with the density-dependent $\delta$ force, paying special attention to the dineutron structure of valence neutrons. We particularly study the Borromean nuclei, $^6$He and $^{11}$Li, and also another drip line nucleus, $^{24}$O, as a comparison. Because $^{23}$O is bound, $^{24}$O is not a Borromean nucleus by definition, although the root-mean-square (rms) radius indicates a feature of very extended neutron wave functions. The model we use is essentially the same as that of Bertsch and Esbensen [1–3], and the interaction is adjusted to fit the separation energy of each drip line nucleus.

The paper is organized as follows. In Sec. II, we discuss the three-body model and the adopted two-body interactions. The results for the Borromean nuclei are compared with those for the drip line nucleus $^{24}$O in Sec. III. A summary is given in Sec. IV.

## II. THREE-BODY MODEL

We consider a three-body system consisting of two valence neutrons and an inert core nucleus with the mass number $A_c$. We use the same three-body Hamiltonian as in Ref. [3], that is,

$$H = \hat{h}_{nC}(1) + \hat{h}_{nC}(2) + V_{nn} + \frac{\boldsymbol{p}_1 \cdot \boldsymbol{p}_2}{A_c m}. \tag{1}$$

Here, $\hat{h}_{nC}$ is the single-particle Hamiltonian for a valence neutron interacting with the core and is given by

$$\hat{h}_{nC} = \frac{p^2}{2\mu} + V_{nC}(r), \tag{2}$$

where $\mu = mA_c/(A_c + 1)$ is the reduced mass. The reduced mass $\mu$, together with the last term in Eq. (1), originates from the recoil kinetic energy of the core [3]. $V_{nn}$ is the interaction between the valence neutrons given by

$$V_{nn}(\boldsymbol{r}_1, \boldsymbol{r}_2) = \delta(\boldsymbol{r}_1 - \boldsymbol{r}_2)\left\{v_0 + \frac{v_\rho}{1 + \exp[(r_1 - R_\rho)/a_\rho]}\right\}. \tag{3}$$

It is well known that $\delta$ force (3) must be supplemented with an energy cutoff $E_{\rm cut}$ in the two-particle spectrum. In terms of the energy cutoff $E_{\rm cut}$ and the scattering length $a_{nn}$ for $nn$ scattering, the strength for the $\delta$ interaction $v_0$ is given by [3]

$$v_0 = \frac{2\pi^2\hbar^2}{m}\frac{2a_{nn}}{\pi - 2k_c\, a_{nn}}, \tag{4}$$

 

where $E_{\rm cut} = \hbar^2 k_c^2/m$. The parameters for the density-dependent part, i.e., $v_\rho$, $R_\rho$, and $a_\rho$, are adjusted in order to reproduce the known ground-state properties for each nucleus. We specify the value of the parameters below.

We diagonalize Hamiltonian (1) in the model space of the two-particle states with the energy $\epsilon_1 + \epsilon_2 \leqslant [(A_c + 1)/A_c]E_{\rm cut}$ [3], where $\epsilon$ is a single-particle energy of the valence particle. We use a Woods-Saxon potential for $V_{nC}$ to generate the single-particle basis:

$$V_{nC}(r) = V_0 \left[1 - 0.44 f_{\rm so} r_0^2 (\boldsymbol{l}\cdot\boldsymbol{s}) \frac{1}{r}\frac{d}{dr}\right] \times \left[1 + \exp\left(\frac{r-R}{a}\right)\right]^{-1}, \quad (5)$$

where $R = r_0 A_c^{1/3}$. For $^6$He, we use the parameter set $a = 0.65$ fm, $r_0 = 1.25$ fm, $V_0 = -47.4$ MeV, and $f_{\rm so} = 0.93$ that reproduces the measured low-energy $n = \alpha$ phase shifts [3]. We employ the same parameters for the density-dependent interaction as those in line 5 of Table II in Ref. [3]: $a_{nn} = -15$ fm, $E_{\rm cut} = 40$ MeV, $v_\rho = -v_0$, $R_\rho = 2.436$ fm, and $a_\rho = 0.67$ fm. The continuum single-particle spectrum is discretized with a radial box of $R_{\rm box} = 30$ fm.

For $^{11}$Li, we use $a = 0.67$ fm, $r_0 = 1.27$ fm, $f_{\rm so} = 1.006$, and $R_{\rm box} = 40$ fm. For the Woods-Saxon potential, a deep potential $V_0 = -47.5$ MeV is used for the even-parity states, whereas a shallow potential $V_0 = -35.366$ MeV is adopted for the odd-parity states in order to increase the $s$-wave component of the ground-state wave function [3]. Similar potentials are used also in Ref. [4]. For the density-dependent force, we use a similar parameter set $a_{nn} = -15$ fm, $E_{\rm cut} = 30$ MeV, $v_\rho = -v_0$, $R_\rho = 2.935$ fm, and $a_\rho = 0.67$ fm to that of line 5 in Table IV in Ref. [3] except the value of the energy cutoff.

For $^{24}$O, we use $V_0 = -43.2$ MeV, $a = 0.67$ fm, $r_0 = 1.25$ fm, $f_{\rm so} = 0.73$, and $R_{\rm box} = 30$ fm so that the bound $s_{1/2}$ and $d_{5/2}$ states have empirical single-particle energies $-2.739$ and $-3.806$ MeV observed in $^{23}$O and $^{21}$O, respectively. For the pairing interaction, we use $a_{nn} = -15$ fm, $E_{\rm cut} = 30$ MeV, $v_\rho = 814.2$ MeV fm$^3$, $R_\rho = R$, and $a_\rho = 0.67$ fm, which reproduce the two-neutron separation energy of $^{24}$O, $S_{2n} = 6.452$ MeV.

The calculated ground-state properties are summarized in Table I, where

$$\langle r_{nn}^2 \rangle = \langle \Psi_{\rm gs} | (\boldsymbol{r}_1 - \boldsymbol{r}_2)^2 | \Psi_{\rm gs} \rangle, \quad (6)$$

is the mean-square distance between the valence neutrons, and

$$\langle r_{c-2n}^2 \rangle = \langle \Psi_{\rm gs} | (\boldsymbol{r}_1 + \boldsymbol{r}_2)^2/4 | \Psi_{\rm gs} \rangle, \quad (7)$$

is the mean-square distance of their center of mass with respect to the core.

TABLE I. Ground-state properties of $^6$He, $^{11}$Li, and $^{24}$O obtained with the three-body model with the density-dependent $\delta$ interaction. The result for $^6$He is the same as that in line 5 of Table II in Ref. [3].

| Nucleus | $S_{2n}$ (MeV) | $\langle r_{nn}^2 \rangle$ (fm$^2$) | $\langle r_{c-2n}^2 \rangle$ (fm$^2$) | Dominant configuration | Fraction (%) | $S = 0$ (%) |
|---|---|---|---|---|---|---|
| $^6$He | 0.975 | 21.3 | 13.2 | $(p_{3/2})^2$ | 83.0 | 87.0 |
| $^{11}$Li | 0.295 | 41.4 | 26.3 | $(p_{1/2})^2$ | 59.1 | 60.6 |
| $^{24}$O | 6.452 | 35.2 | 10.97 | $(s_{1/2})^2$ | 93.6 | 97.7 |

## III. DISCUSSIONS

### A. Ground-state properties

Let us now discuss the spatial correlation of the valence neutrons in the ground state and its influence on the dipole excitations near the neutron threshold. To this end, we first plot the two-particle density. It is given as a function of two radial coordinates, $r_1$ and $r_2$, for the valence neutrons, and the angle between them, $\theta_{12}$. The two-particle density can be decomposed into the $S = 0$ and $S = 1$ components in the $LS$-coupling scheme, i.e.,

$$\rho_2(r_1, r_2, \theta_{12}) = \rho_2^{S=0}(r_1, r_2, \theta_{12}) + \rho_2^{S=1}(r_1, r_2, \theta_{12}). \quad (8)$$

The explicit expression for the each component is given by [1]

$$\rho_2^{S=0}(r_1, r_2, \theta_{12}) = \frac{1}{8\pi} \sum_L \sum_{l,j} \sum_{l',j'} \frac{\hat{l}\hat{l}'\hat{L}}{\sqrt{4\pi}} \begin{pmatrix} l & l' & L \\ 0 & 0 & 0 \end{pmatrix}^2 \times \Phi_{lj}(r_1, r_2)\Phi_{l'j'}(r_1, r_2) Y_{L0}(\theta_{12}) \times (-)^{l+l'} \sqrt{\frac{2j+1}{2l+1}} \sqrt{\frac{2j'+1}{2l'+1}}, \quad (9)$$

$$\rho_2^{S=1}(r_1, r_2, \theta_{12}) = \frac{1}{8\pi} \sum_L \sum_{l,j} \sum_{l',j'} \frac{\hat{l}\hat{l}'\hat{L}}{\sqrt{4\pi}} \times \begin{pmatrix} l & l' & L \\ 0 & 0 & 0 \end{pmatrix} \begin{pmatrix} l & l' & L \\ 1 & -1 & 0 \end{pmatrix} \times \Phi_{lj}(r_1, r_2)\Phi_{l'j'}(r_1, r_2) Y_{L0}(\theta_{12}) \times (-)^{j+j'} \sqrt{2 - \frac{2j+1}{2l+1}} \times \sqrt{2 - \frac{2j'+1}{2l'+1}}, \quad (10)$$

where $\hat{l} = \sqrt{2l+1}$. Here, $\Phi_{lj}(r, r')$ is the radial part of the two-particle wave function defined as

$$\Phi_{lj}(r, r') = \sum_{n' \leqslant n} \frac{\alpha_{nn'lj}}{\sqrt{2(1+\delta_{n,n'})}} \times [\phi_{nlj}(r)\phi_{n'lj}(r') + \phi_{nlj}(r')\phi_{n'lj}(r)], \quad (11)$$

where $n$ and $n'$ are the radial quantum numbers, $\alpha_{nn'lj}$ is the expansion coefficient, and $\phi_{nlj}(r)$ is the radial part of the Woods-Saxon single-particle wave function. Note that the two-particle density is normalized as

$$\int_0^\infty 4\pi r_1^2\, dr_1 \int_0^\infty r_2^2\, dr_2 \int_0^\pi 2\pi \sin\theta_{12}\, d\theta_{12} \rho_2(r_1, r_2, \theta_{12}) = 1. \quad (12)$$

Figures 1, 2, and 3 show the (total) two-particle density (the top panels) for the $^6$He, $^{11}$Li, and $^{24}$O nuclei, respectively, and their spin decompositions (the middle and the bottom panels). These are plotted as functions of the radius $r_1 = r_2 \equiv r$ and the angle $\theta_{12}$, and with a weight of $4\pi r^2\, 2\pi r^2 \sin\theta_{12}$.

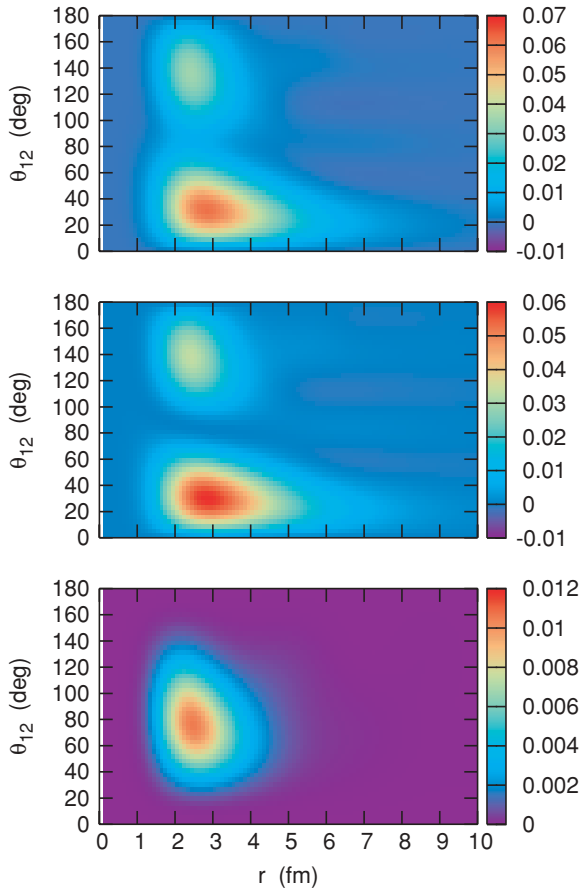


FIG. 1. (Color online) The two-particle density for $^6$He as a function of $r_1 = r_2 = r$ and the angle between the valence neutrons, $\theta_{12}$. It is weighted with a factor of $4\pi r^2\, 2\pi r^2 \sin\theta_{12}$. The top panel shows the total density, and the middle and the bottom panels show the $S = 0$ and the $S = 1$ components in the $LS$-coupling scheme, respectively.

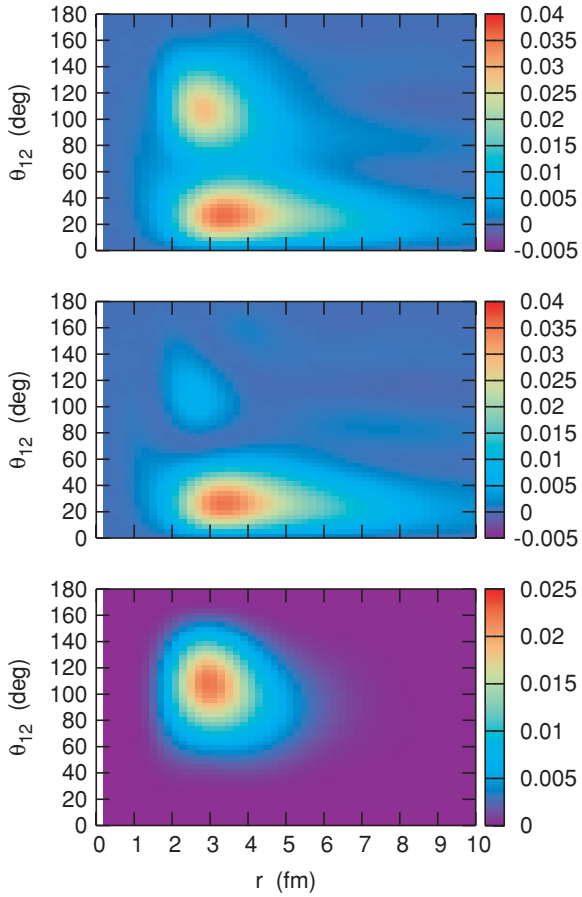


FIG. 2. (Color online) Same as Fig. 1, but for $^{11}$Li.

As has been pointed out in Refs. [1,6,12], one observes two-peaks in the two-particle densities, although the two-peaked structure is somewhat smeared in $^{24}$O. The peaks at smaller and larger $\theta_{12}$ are referred to as "dineutron" and "cigarlike" configurations in Refs. [6,12], respectively. We see that the dineutron part of the two-particle density has a long radial tail in $^6$He and $^{11}$Li, and thus can be interpreted as a halo structure. In contrast, the cigarlike configuration has a rather compact radial shape. For $^{24}$O, the dineutron and the cigarlike configurations behave similarly as functions of $r$ and do not show a halo structure. Evidently, a large rms radius of $^{24}$O is attributed to the dominant $s$-wave component in the ground-state wave function, rather than the halo effect (see below).

We find that the spin structure of the two-particle density is considerably different among the three nuclei studied. To see this transparently, we introduce the angular density $\rho(\theta_{12})$ by integrating the radial coordinates in the two-particle density, i.e.,

$$\rho(\theta_{12}) \equiv 4\pi \int_0^\infty r_1^2\, dr_1 \int_0^\infty r_2^2\, dr_2 \rho_2(r_1, r_2, \theta_{12}). \quad (13)$$

The angular density is normalized to unity as

$$2\pi \int_0^\pi \sin\theta_{12}\, d\theta_{12}\, \rho(\theta_{12}) = 1. \quad (14)$$

Figure 4 shows the angular density for the $^6$He, $^{11}$Li, and $^{24}$O (with a weight of $2\pi \sin\theta_{12}$). The solid curve is the total density, whereas the dashed and the dotted curves are for the $S = 0$ and the $S = 1$ components, respectively. The fraction for the $S = 0$ component is 87.0%, 60.6%, and 97.7% for $^6$He, $^{11}$Li, and $^{24}$O, respectively. The expectation value of the angle $\theta_{12}$ is 66.33°, 65.29°, and 82.37° for $^6$He, $^{11}$Li, and $^{24}$O, respectively. For the Borromean nuclei $^6$He and $^{11}$Li, the $S = 0$ wave function dominates the dineutron part of the two-particle density. In contrast, the cigar-like part has a large $S = 1$ part in $^{11}$Li, but still the $S = 0$ component dominates in $^6$He. For the $^{24}$O nucleus, there is no clear separation between the dineutron- and the cigarlike-type structures. The wave function shows a strong correlation typical in the BCS type wave function [13,14]. In fact, the calculated rms radius for $^{24}$O, 4.45 fm, is close to that of the bound $2s_{1/2}$ state, 4.65 fm. A small difference in the rms radii is due to the antihalo effect discussed in Ref. [15], in which the pairing correlation tends to decrease the value of rms radius as compared with the case without the pairing correlation.

The main features of the angular dependence of the two-particle density shown in Fig. 4 can be understood in the

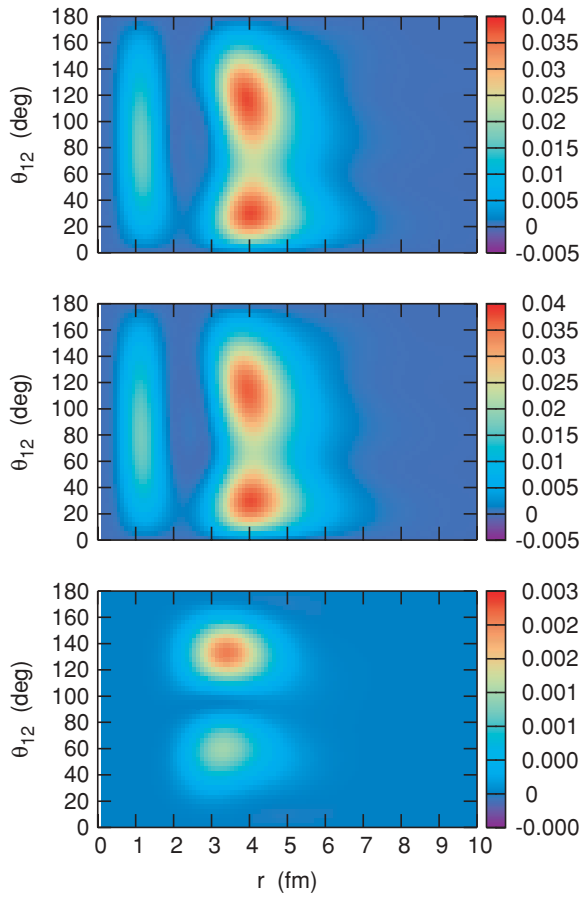


FIG. 3. (Color online) Same as Fig. 1, but for $^{24}$O.

following way. From Eqs. (9) and (10), one can obtain by inserting the values of $3j$ symbols that

$$\rho^{S=0}(\theta_{12}) \propto \frac{1}{3}Y_{00}(\theta_{12}) + \frac{2\sqrt{5}}{15}Y_{20}(\theta_{12}) \propto \cos^2\theta_{12}, \quad (15)$$

$$\rho^{S=1}(\theta_{12}) \propto \frac{1}{3}Y_{00}(\theta_{12}) - \frac{5}{\sqrt{15}}Y_{20}(\theta_{12}) \propto \sin^2\theta_{12}, \quad (16)$$

for the configurations $(j,l) = (j',l') = p_{3/2}$ or $(j,l) = (j',l') = p_{1/2}$. When weighted by $\sin\theta_{12}$, Eq. (15) has a peak at $\theta_{12} = 35.26^\circ$ and $144.74^\circ$, whereas Eq. (16) has the maximum at $\theta_{12} = 90^\circ$. This is indeed the case for the $^6$He nucleus. For the $^{11}$Li, the admixture of the $(s_{1/2})^2$ and $(d_{5/2})^2$ configurations perturb this picture, and a peak at $\theta_{12} = 144.74^\circ$ in the $S = 0$ component disappears to a large extent. For the $^{24}$O nucleus, the $S = 1$ component is largely suppressed because the pure $(s_{1/2})^2$ state cannot form the $S = 1$ configuration. Also, the two-particle density for the pure $(s_{1/2})^2$ configuration is proportional to $|Y_{00}|^2$, and thus has a peak at $\theta_{12} = 90^\circ$ when it is weighted by $\sin\theta_{12}$.

### B. Dipole excitations

We next discuss the response of the ground state to the dipole field,

$$\hat{D}_M = -\frac{Z}{A}e[r_1 Y_{1M}(\hat{\boldsymbol{r}}_1) + r_2 Y_{1M}(\hat{\boldsymbol{r}}_2)]. \quad (17)$$

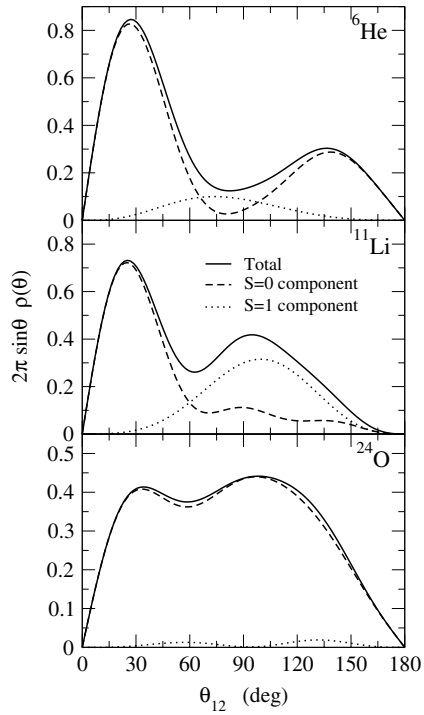


FIG. 4. The angular density defined by Eq. (13) (weighted with a factor $2\pi\sin\theta$) for $^6$He, $^{11}$Li, and $^{24}$O. The solid line is for the total density, while the dashed and the dotted lines are for the $S = 0$ and the $S = 1$ components in the $LS$-coupling scheme, respectively.

Because we obtain the excited $1^-$ states by matrix diagonalization, they appear as discrete states. We smear the discrete strength distribution with a smearing function as

$$B(E1) = \sum_k \frac{\Gamma}{\pi}\frac{1}{(E-E_k)^2+\Gamma^2}B_k(E1), \quad (18)$$

where $B_k(E1)$ is the $B(E1)$ strength for the $k$th excited state:

$$B_k(E1) = 3\left|\langle\Psi^k_{1^-}|\hat{D}_0|\Psi_{\rm gs}\rangle\right|^2. \quad (19)$$

Figure 5 shows the $B(E1)$ distributions for the $^6$He, $^{11}$Li, and $^{24}$O. The solid and the dashed lines are obtained with smearing function (18) with $\Gamma = 0.2$ and 0.5 MeV, respectively. The discrete distributions are also shown. The total $B(E1)$ strengths, $\sum_k B_k(E1)$, are 1.31, 1.76, and 0.97 $e^2$ fm$^2$ for $^6$He, $^{11}$Li, and $^{24}$O, respectively.

We note that strong threshold peaks appear in the responses of $^6$He and $^{11}$Li. In the cluster model within the plane-wave approximation, the peak of the strength function appears at $1.6S_c$, where $S_c$ is the cluster separation energy [16–18]. The calculated peaks in Fig. 5 are at 1.55 and 0.66 MeV for $^6$He and $^{11}$Li, respectively. These peaks are very close to 1.6 times the two-neutron separation energy, $1.6S_{2n} = 1.56$ MeV for $^6$He and 0.47 MeV for $^{11}$Li. This similarity suggests the existence of strong dineutron correlations in these nuclei. A small difference between the peak energy in Fig. 5 and $1.6S_{2n}$ for $^{11}$Li is due to the large configuration mixing of the $s_{1/2}$ state (22.7%) in the ground state. In contrast, for $^{24}$O, the peak (4.78 MeV) is below the two-neutron separation energy and is rather close to 1.6 times the single-particle energy for the

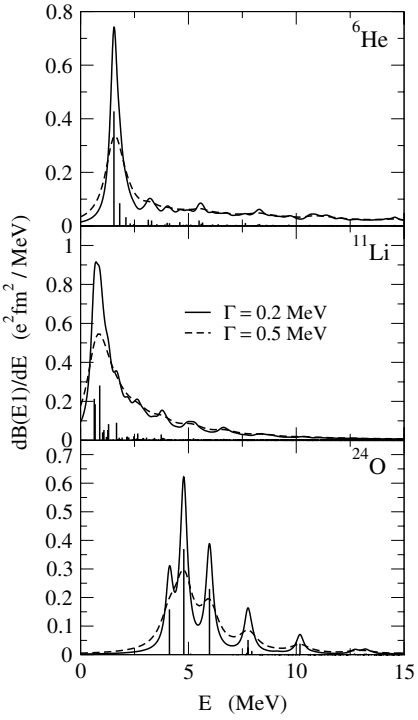


FIG. 5. The $B(E1)$ distribution for $^6$He, $^{11}$Li, and $^{24}$O. The solid and the dashed lines are obtained with a smearing procedure with $\Gamma = 0.2$ and 0.5 MeV, respectively.

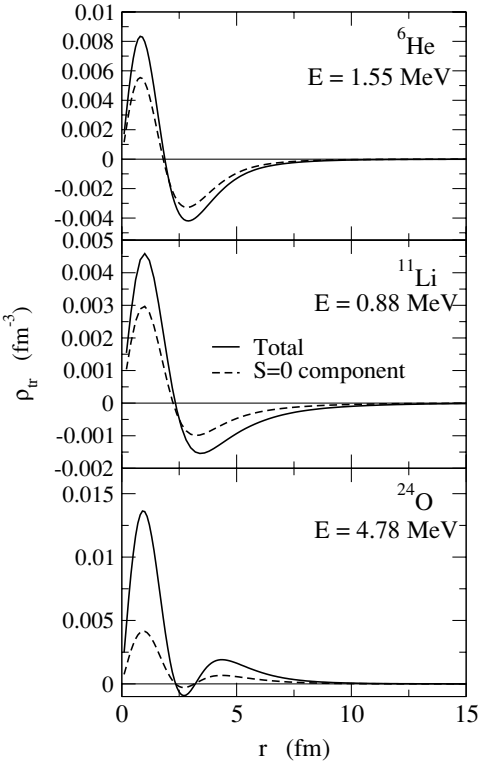


FIG. 6. The transition density for the state close to the peak in the the $B(E1)$ distribution. The top, middle, and bottom panels are for $^6$He, $^{11}$Li, and $^{24}$O, respectively. The solid line indicates the total density, while the $S = 0$ component is denoted by the dashed line.

$2s_{1/2}$ state, that is, $1.6\times\ 2.74 = 4.38$ MeV. Therefore the dineutron correlation does not seem to play a major role in the dipole response in this nucleus.

To see the threshold effect more clearly, we plot in Fig. 6 the transition density for the strong $E1$ peaks for each nucleus. As a comparison, we also show the $S = 0$ component of the transition density by the dashed curves. For $^6$He and $^{11}$Li, the transition density shows a nodal structure and changes its sign, which is typical in the coupling to the continuum spectrum. Also, the $S = 0$ component plays a significant role, supporting the importance of the dineutron correlation in these nuclei. On the other hand, such a clear nodal structure is not seen in the transition density of $^{24}$O. The transition density seems to consist of a coherent sum of the $S = 0$ and the $S = 1$ components. The dipole excitation in $^{24}$O is therefore interpreted as a coherent superposition of particle-hole excitations, rather than continuum excitations, as in stable nuclei in which the continuum effect is much less important.

We mention that, although the Coulomb breakup for the one-neutron halo $^{11}$Be is now well established, that for the two-neutron halo $^{11}$Li is still in dispute, showing large discrepancies among the experimental data taken by three different groups [19]. Recently, Nakamura performed the Coulomb dissociation experiments of $^{11}$Li on a $^{208}$Pb target with much higher statistics and with much less ambiguities caused by cross-talk events in detecting two neutrons [20]. They observed a sharp peak at $E_{\rm exp} \sim 0.6$ MeV and the integrated strength $B_{\rm exp}(E1) = 1.5 \pm 0.1\, e^2$ fm$^2$ for $E < 3.3$ MeV, which are consistent with the present results, $E_{\rm peak} = 0.66$ MeV with the calculated strength $B_{\rm cal}(E1) = 1.31\, e^2$ fm$^2$ for $E < 3.3$ MeV. Similar calculated results were also reported in Ref. [2], although Ref. [2] did not take into account the effect of the recoil of the core and setted the *nn* scattering length to be infinite. Our calculation is an improvement on that of Ref. [2] as we include the core recoil effect and use the realistic value for the *nn* scattering length.

## IV. SUMMARY

We have studied the role of dineutron correlations in weakly bound nuclei on the neutron-drip line by using a three-body model. The model Hamiltonian consists of a Woods-Saxon potential between a valence neutron and the core and of a density-dependent pairing interaction among the valence neutrons. We applied this model to the Borromean nuclei, $^6$He and $^{11}$Li, as well as a skin nucleus $^{24}$O. For the Borromean nuclei, $^6$He and $^{11}$Li, we found that the two-particle density has a two-peaked structure, one peak at a small opening angle between the valence neutrons and the other at a large angle (the dineutron and cigarlike configurations, respectively). We found that the former is dominated by the $S = 0$ configurations in the *LS*-coupling scheme and has a long tail. On the other hand, the latter has a compact shape and is dominated by the $S = 1$ configuration for $^{11}$Li and by the $S = 0$ configuration for $^6$He. For $^{24}$O, there is no clear separation between the dineutron and the cigarlike configurations, and the ground state is dominated by the $S = 0$ configuration.

We have also studied the dipole response of these nuclei within the same model. We found strong threshold peaks in the responses of $^{6}$He and $^{11}$Li nuclei, in which the transition density shows the importance of the coupling to the continuum. The $S = 0$ configuration and thus the dineutron correlation were found to make a large contribution to the transition density for these peaks. On the other hand, no clear sign of the continuum coupling was seen in the response of $^{24}$O. The transition density for the low-energy dipole strength of $^{24}$O consists of a coherent sum of the $S = 0$ and the $S = 1$ components, and therefore the dineutron correlation plays a much less important role in $^{24}$O than in the Borromean nuclei.

Recently, a new Coulomb breakup measurement for $^{11}$Li has been undertaken at RIKEN [20]. It would be interesting to perform a similar experiment also for the $^{24}$O nucleus and see a difference between them, as we discussed in this paper.

## ACKNOWLEDGMENTS

This work was supported by the Japanese Ministry of Education, Culture, Sports, Science and Technology by Grant-in-Aid for Scientific Research under the program numbers (C(2)) 16540259 and 16740139.

[1] G. F. Bertsch and H. Esbensen, Ann. Phys. (NY) **209**, 327 (1991).
[2] H. Esbensen and G. F. Bertsch, Nucl. Phys. **A542**, 310 (1992).
[3] H. Esbensen, G. F. Bertsch, and K. Hencken, Phys. Rev. C **56**, 3054 (1999).
[4] N. Vinh Mau and J. C. Pacheco, Nucl. Phys. **A607**, 163 (1996).
[5] A. Bonaccorso and N. Vinh Mau, Nucl. Phys. **A615**, 245 (1997).
[6] M. V. Zhukov *et al*., Phys. Rep. **231**, 151 (1993).
[7] D. V. Fedorov, E. Garrido, and A. S. Jensen, Phys. Rev. C **51**, 3052 (1995).
[8] B. S. Pudliner, V. R. Pandharipande, J. Carlson, and R. B. Wiringa, Phys. Rev. Lett. **74**, 4396 (1995); S. C. Pieper, V. R. Pandharipande, R. B. Wiringa, and J. Carlson, Phys. Rev. C **64**, 014001 (2001).
[9] M. Matsuo, K. Mizuyama, and Y. Serizawa, Phys. Rev. C **71**, 064326 (2005).
[10] S. Aoyama, K. Kato, and K. Ikeda, Prog. Theor. Phys. Suppl. **142**, 35 (2001); T. Myo, S. Aoyama, K. Kato, and K. Ikeda, Prog. Theor. Phys. **108**, 133 (2002).
[11] T. Myo, S. Aoyama, K. Kato, and K. Ikeda, Phys. Lett. **B576**, 281 (2003); T. Myo, K. Kato, S. Aoyama, and K. Ikeda, Phys. Rev. C **63**, 054313 (2001).
[12] Yu. Ts. Oganessian, V. I. Zagrebaev, and J. S. Vaagen, Phys. Rev. Lett. **82**, 4996 (1999); Phys. Rev. C **60**, 044605 (1999).
[13] P. Ring and P. Schuck, *The Nuclear Many Body Problem* (Springer-Verlag, New York, 1980).
[14] M. Grasso, N. Sandulescu, N. V. Giai, and R. J. Liotta, Phys. Rev. C **64**, 064321 (2001).
[15] K. Bennaceur, J. Dobaczewski, and M. Ploszajczak, Phys. Lett. **B496**, 154 (2000).
[16] H. Sagawa, N. Takigawa, and Nguyen Van Giai, Nucl. Phys. **A543**, 575 (1992).
[17] C. A. Bertulani, G. Baur, and M. S. Hussein, Nucl. Phys. **A526**, 751 (1991).
[18] K. Hagino, M. S. Hussein, and A. B. Balantekin, Phys. Rev. C **68**, 048801 (2003).
[19] K. Ieki *et al*., Phys. Rev. Lett. **70**, 730 (1993); S. Shimoura *et al*., Phys. Lett. **B348**, 29 (1995); M. Zinser *et al*., Nucl. Phys. **A619**, 151 (1997).
[20] T. Nakamura and N. Fukuda, Eur. Phys. J. A **25**, Suppl. 1, 325 (2005).